Effective catalysis and antibacterial activity of silver and gold nanoparticles biosynthesized by *Phlogacanthus turgidus*

Van-Su Dang[1] · Hoang-Huy Tran[2] · Phan Thi Thanh Dieu[1] · Minh-Trong Tran[2,3] · Chi-Hien Dang[2,3] · Dinh-Tri Mai[2,3] · Van-Dat Doan[4] · Thi-Lan-Huong Nguyen[5] · Tran Thi Kim Chi[6] · Thanh-Danh Nguyen[2,3]

Abstract

In this work, an environmentally friendly and cost-effective synthetic method of silver nanoparticles (AgNPs) and gold nanoparticles (AuNPs) was successfully performed using aqueous extract of *Phlogacanthus turgidus* (PT) leaves. The biosynthesis of nanoparticles was optimized for reaction conditions including concentration of metallic ions, temperature, and time using the measurement of UV–Vis spectroscopy. The nanoparticles were well characterized by analytic techniques such as Fourier-transform infrared (FTIR) spectroscopy, X-ray diffraction (XRD), high-resolution transmission electron microscope (HR-TEM), and selected area electron diffraction (SAED). The morphological data showed that PT-AgNPs possessed the spherical shape with the size distribution ranging from 5 to 15 nm with a mean size of 10 nm while PT-AuNPs existed in the multiple shape with the size distribution ranging from 5 to 20 nm with a mean size of 12 nm. The antibacterial behavior showed that PT-AgNPs possessed high bioactivity against four bacterial strains including *Bacillus subtilis*, *Staphylococcus aureus, Salmonella typhi*,

✉ Thanh-Danh Nguyen
ntdanh@ict.vast.vn

1 Department of Chemical Technology, Ho Chi Minh City University of Food Industry, Ho Chi Minh City, Vietnam

2 Institute of Chemical Technology, Vietnam Academy of Science and Technology, 1A, TL29, Thanh Loc Ward, District 12, Ho Chi Minh City, Vietnam

3 Graduate University of Science and Technology, Vietnam Academy of Science and Technology, 18 Hoang Quoc Viet, Cau Giay District, Hanoi, Vietnam

4 Faculty of Chemical Engineering, Industrial University of Ho Chi Minh City, 12 Nguyen Van Bao, Ho Chi Minh City, Vietnam

5 Institute of Biotechnology and Food Technology, Industrial University of Ho Chi Minh City, 12 Nguyen Van Bao, Ho Chi Minh City, Vietnam

6 Institute of Materials Science, Vietnam Academy of Science and Technology, 18 Hoang Quoc Viet, Cau Giay District, Hanoi, Vietnam

and *Escherichia coli.* Moreover, the catalytic activity of the biogenic nanoparticles was investigated for catalytic reduction of 2-nitrophenol, 3-nitrophenol, and rhodamine B. The kinetic data showed that the nanoparticles were excellent catalysts with potential applications for environmental treatment.

Graphical abstract

Introduction

Recently, metallic nanoparticles are particularly interested for multiple applications in the various fields including pharmaceutical technology [1, 2], catalysis [3–5], and chemical sensors [6, 7]. The green synthetic method of metallic nanoparticles using natural sources (e.g., microbial, embryos and plant extracts) is an alternative approach to chemical and physical synthesis which uses the harmful chemicals and expensive techniques [8–10]. In particular, the phytochemicals in the aqueous

plant extract are well known as the reducing and stabilizing agents for the synthesis of nanomaterials [11]. The eco-friendly organic layers around nanometals can significantly reduce toxicity of the metallic nanoparticles in biological applications [12–16]. Thus, the biosynthesized nanometals are used as antimicrobial agents that can be effectively applied for medicine and agriculture. Moreover, due to low cost and simple synthetic process, the biogenic metallic nanoparticles are considered for catalytic reduction and degradation of hazardous chemicals from the wastewater [5, 17].

Numerous toxic organic dyes such as nitrophenols (NiPs) and rhodamine B (RhB) cause water pollution. Many treatment methods like adsorption, degradation, and filtration have been used to remove these contaminants [18, 19]. Among them, the catalytic reduction is frequently explored for the treatment of industrial wastewater. Particularly, the reduction of NiPs into relative aminophenols (APs) using nanocatalyst are widely investigated since NiPs possess high stability in water medium. Moreover, the APs products are important intermediates for the synthesis of many analgesic and antipyretic drugs [20, 21]. APs are also utilized as corrosion inhibitors in paints, anticorrosion-lubricating agents in fuels, and dyeing agents for feather and fur [22, 23]. Many previous studies demonstrated that plasmonic nanometals (e.g., AgNPs and AuNPs) biosynthesized from plant extract are the potential catalysts for degradation of these organic contaminants due to environmentally friendly property, low cost, and large-scale application [24–28].

Phlogacanthus turgidus (PT) is a flowering plant in the family Hydrangeaceae living in China and Southeast Asia including Thailand, Indonesia, Myanmar, and Vietnam. PT is cultivated as an ornamental and a medicinal plant [29]. For medicinal property, it possesses various bioactivity such as antioxidant and acute toxicity. PT contains alkaloids, proteins, phenolic compounds, saponins, terpenoids, flavonoids, and glycosides [30, 31] which can be responsible for the biosynthesis of nanometals. To the best of our knowledge, the aqueous extract of PT leaves has not been used for the fabrication of nanoparticles.

In the present work, AgNPs and AuNPs were biosythesized using phytoconstituents in aqueous extract of PT leaves as reducing and stabilizing agents. The nanoparticles have been optimized to determine suitable synthesis condition. The nanoparticles have been investigated for antibacterial effects and catalytic activity for reduction of NiPs and RhB in water medium.

Materials and methods

Chemicals

Chemicals including hydrogen tetrachloroaurate (III) hydrate ($HAuCl_4 \cdot 3H_2O$), silver nitrate ($AgNO_3$), 2-nitrophenol (2-NiP), 3-nitrophenol (3-NiP), and rhodamine B (RhB) used in analytical grade without further purification were purchased from Acros Co, Belgium. The deionized water was thoroughly utilized in all experiments.

For the preparation of PT extract, 10 g of dried PT powder was boiled in 100 mL of water for 2 h. The mixture was filtered to remove the solid and water was added to

afford 100 mL of PT extract. For further studies, the resulting filtrates were stored at 4 °C in a refrigerator.

Synthesis of biogenic nanoparticles

PT extract was utilized as a reducing and stabilizing agent for the fabrication of metallic nanoparticles which was carried out under dark condition. Briefly, 0.25 mL of PT extract was added to aqueous solution of metallic ions (5 mL) and the mixture was stirred at 1000 rpm. The reaction conditions including metallic ion concentration, temperature, and time were optimized using UV–Vis measurement with a UV–Vis Evolution 300 spectrophotometer. The changes in absorbance and surface plasmon resonance (SPR) absorption peaks allowed to evaluate the nanoparticle formation. For further studies, the nanoparticles fabricated under the optimal conditions were used. The solid nanoparticles used for physicochemical characterizations were obtained from centrifugal process at 4,000 rpm for 30 min, washed with water and ethanol, and then dried overnight at 60 °C.

Physicochemical characterizations

The solution of biogenic nanoparticles was determined zeta potential on the sliding plane and dynamic light scattering (DLS) using a nanoPartica Horiba SZ-100 (Japan). Fourier-transform infrared spectroscopy (FTIR) spectra were used to identify possible functional groups as stabilizing agents in solid nanoparticles which were recorded via a Bruker Tensor 27 (Germany) in range of 4000–500 cm^{-1}. Crystalline structures of biogenic nanoparticles were analyzed for powder X-ray diffraction (XRD) using a Shimadzu 6100 X-ray diffractometer (Japan) which operated at the current of 30 mA, the voltage of 40 kV with CuKα radiation at wavelength of 1.5406 nm. Size distribution and morphological characterization of the nanoparticle solutions were determined by scanning electron microscope (SEM), transmission electron microscope (TEM), high-resolution transmission electron microscope (HR-TEM), and the selected area electron diffraction pattern (SAED) using JEOL, JEM2100.

Antibacterial activity

The antibacterial activity was performed via the disk diffusion method [32]. Briefly, the colloidal solution of metallic nanoparticles was diluted at different volume ratios of nanoparticles solution to DMSO (1:1; 1:2; 1:4, and 1:8, v/v). Two Gram-positive bacteria (*Bacillus subtilis* and *Staphylococcus aureus*) and two Gram-positive bacteria (*Salmonella typhi* and *Escherichia coli*) were used for the biotest. 20 μL of each aliquot was added to paper disks with 5.5 mm diameter. All disks were placed on the agar plates previously spread with the bacterial culture (1.0 mL, 10^6 CFU/mL). The Luria Bertani broth and antibiotic ampicillin (0.01 mg/mL) were used as negative and positive controls, respectively. The PT extract was also evaluated using the

similar procedure. The activity was recorded via diameters of inhibition zones in millimeters.

Catalytic activity

The catalytic reduction of NiPs and RhB was performed using excess amount of $NaBH_4$ in the presence of nanocatalyst. Briefly, a mixture of the pollutant (2.5 mL, 0.5 mM) and $NaBH_4$ (0.5 mL, 0.25 M) was prepared in a cuvette with a 1.0 cm length. Then, the solution of biosynthesized nanoparticles at different volumes (1 μL – 5 μL) was added into the solution. The UV–Vis measurement was in situ performed from cuvette. The catalytic performance of the reductions was evaluated via kinetic studies using degradation of absorbance values at the relative wavelength.

Results and discussion

Biosynthesis of nanoparticles

Phytochemicals in PT such as alkaloids, flavonoids, phenolic compounds, saponins, steroids, tannins, protein, and glycosides exhibited a good antioxidant activity [30, 31] that can be responsible for the biogenic synthesis of metallic nanoparticles without the toxic chemicals used in production process. The formation of nanoparticles in colloidal solution involves a mechanism of three main stages concluding reduction process of metallic ions, a clustering formation, and growth of nanometals [33]. Each stage is mainly affected by the components and amount of reducing and stabilizing agents in the plant extract. Indeed, the presence of hydroxyl groups in flavonoid compounds can improve the performance of metallic ion reduction while hydroxyl groups in polysaccharide chains and amide groups in protein can effectively stabilize the formed nanoparticles leading to growth of metallic clusters [10]. In the present work, the aqueous extract of PT leaves was used as a green source for the synthesis of nanometals. The study route is illustrated in Fig. 1. The dried leaves
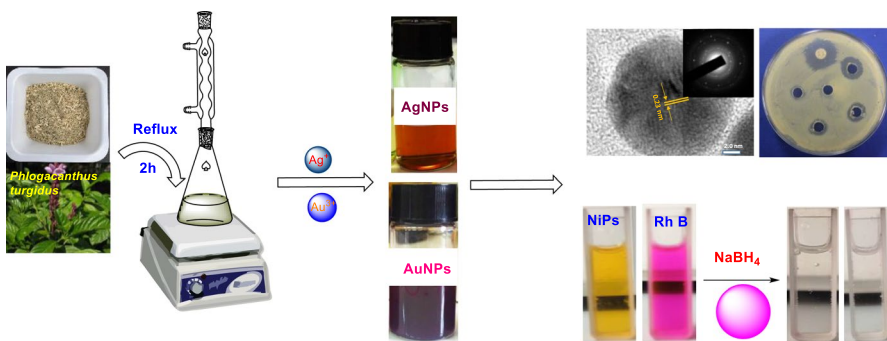

Fig. 1 Schematic illustration of the biosynthesis of metallic nanoparticles and their applications for the antibacterial activity and degradation of toxic compounds

were refluxed with the deionized water in 2 h, affording a yellow solution after the filtration process. The reduction of metallic ions into nanoparticles was optimized to find the suitable conditions for the fabrication of stable colloidal solutions. Changes in color of the solutions confirmed the good conversion of metallic ions to nanoparticles. Moreover, the increase in the absorption intensity at surface plasmon resonance (SPR) peaks was also observed at between 410 and 430 nm for PT-AgNPs and 530–550 nm for PT-AuNPs. The nanometals synthesized under optimal conditions were used to study on physicochemical characterization and their applications for antibacterial and catalytic effects.

The principal reaction conditions including metallic ion concentration, temperature, and time were optimized using UV–Vis spectroscopy that may evaluate changes in concentration, size, and morphology of obtained nanometals via λ_{max} and absorbance at the SPR peak. Figures 2 and 3 describe the absorption spectra and changes in λ_{max} and absorbance values against the investigated parameters of PT-AgNPs and PT-AuNPs, respectively. The result shows different trends in change of absorption parameters, indicating that the metallic nanoparticles formed are strongly dependent on the synthesis conditions.

The formation of PT-AgNPs is strongly influenced by silver ion concentrations as clearly observed in Fig. 2A and 2B. The solution color was changed from yellow to red when the silver ion concentrations were ranged from 0.5 to 2.5 mM. The SPR peak with weak intensity was observed at concentration of 0.5 mM. Content of PT-AgNPs formed in colloidal solutions was gradually increased with increasing concentrations of silver ion in the range of 0.5–2.5 mM and achieved a maximum intensity at 2.0 mM. On the other hand, no significant change in λ_{max} values with increasing silver ion concentrations was observed. It confirms insignificant change in the morphology of the synthesized AgNPs. Thus, the suitable silver ion concentration for the synthesis of stable AgNPs was found to be 2.0 mM.

For the effect of reaction temperature, the reduction of silver ion was investigated ranging from 30 to 80 °C (Fig. 2C and D). The temperature-dependent synthesis of PT-AgNPs is obviously seen by color change of the colloidal solution from yellow to dark brown. The reduction of silver ions was not recognized at around room temperature which was confirmed by the disappearance of SPR peak in UV–Vis spectrum. The absorption intensity is gradually increased with higher temperatures in the range of 50–80 °C. The change of wavelength in a range of 420 to 431 nm indicated nanoparticle formation dependent on reaction temperature. The optimal temperature for the synthesis of PT-AgNPs was determined at 80 °C.

The time-dependent synthesis of PT-AgNPs was optimized in the range of 10–90 min. The formation of PT-AgNPs in the colloidal solution rapidly occurs even at 10 min which exhibits the effective reduction of PT extract compared with the other plant extract reported previously [34, 35]. The absorption intensity at the SPR peak increased with reaction time, indicating the increasing concentration of the AgNPs in the colloidal solution and a maximum content of the nanoparticles was found at 70 min. Moreover, stable λ_{max} values around 413 nm confirmed the independence of morphology on the reaction time.

In the similar way, the optimization of these factors was performed for the synthesis of PT-AuNPs. For the influence of gold ion concentrations, higher gold ion
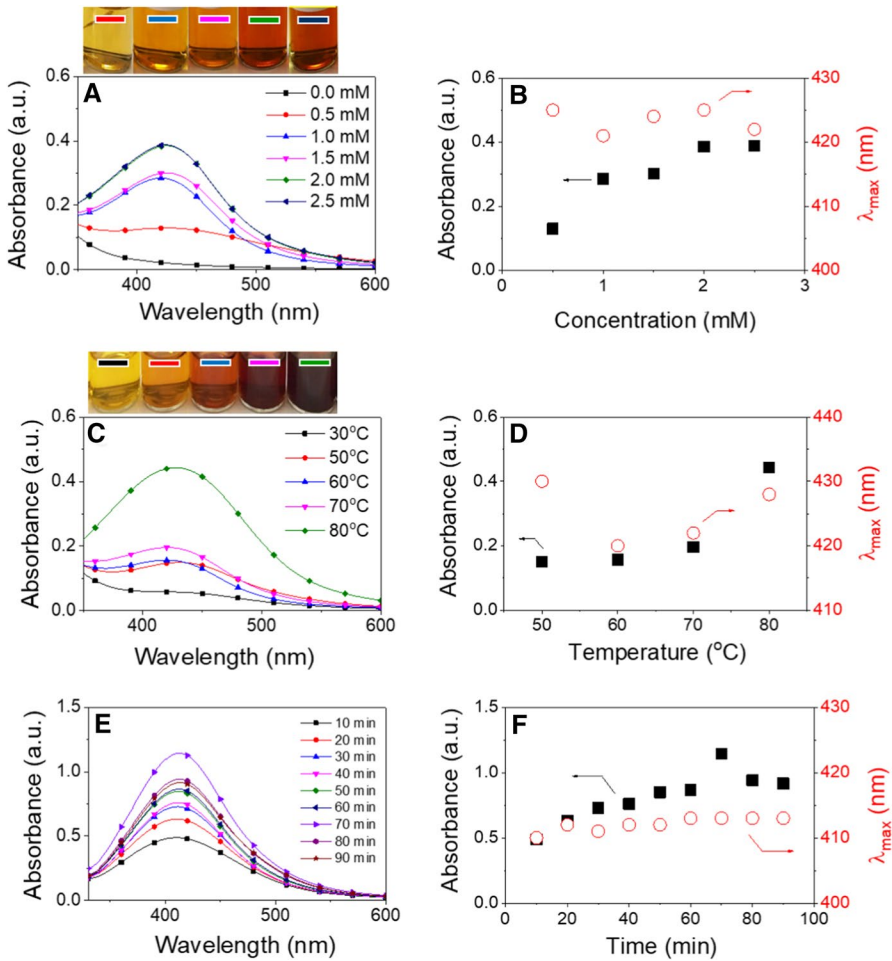
Fig. 2 UV–Vis spectra (left) and relative color change (upper photographs) and plots of parameters versus absorbance and wavelength values (right): concentration of silver ions (**A**, **B**), reaction temperature (**C**, **D**), and reaction time (**E**, **F**) for the biosynthesis of PT-AgNPs

concentrations in range of 0.1–1.0 mM induced increase of PT-AuNPs concentration in colloidal solution which can be confirmed by changes in solution color from yellow to dark red (Fig. 3A and B). A rapid increase in both the absorbance and the λ_{max} values was observed and achieved a maximum value at gold ion concentration of 0.7 mM. After the optimal value, the content of PT-AuNPs is significantly reduced which can relate to excess of stabilizing ability of organic components presented in PT extract, leading to the aggregation of the nanoparticles in the colloidal solution.

The optimization of the reaction temperature was investigated in the range of 30–80 °C (Fig. 3C and D). The formation of AuNPs can be recognized at room temperature with change in solution color and the appearance of intense SPR peak in
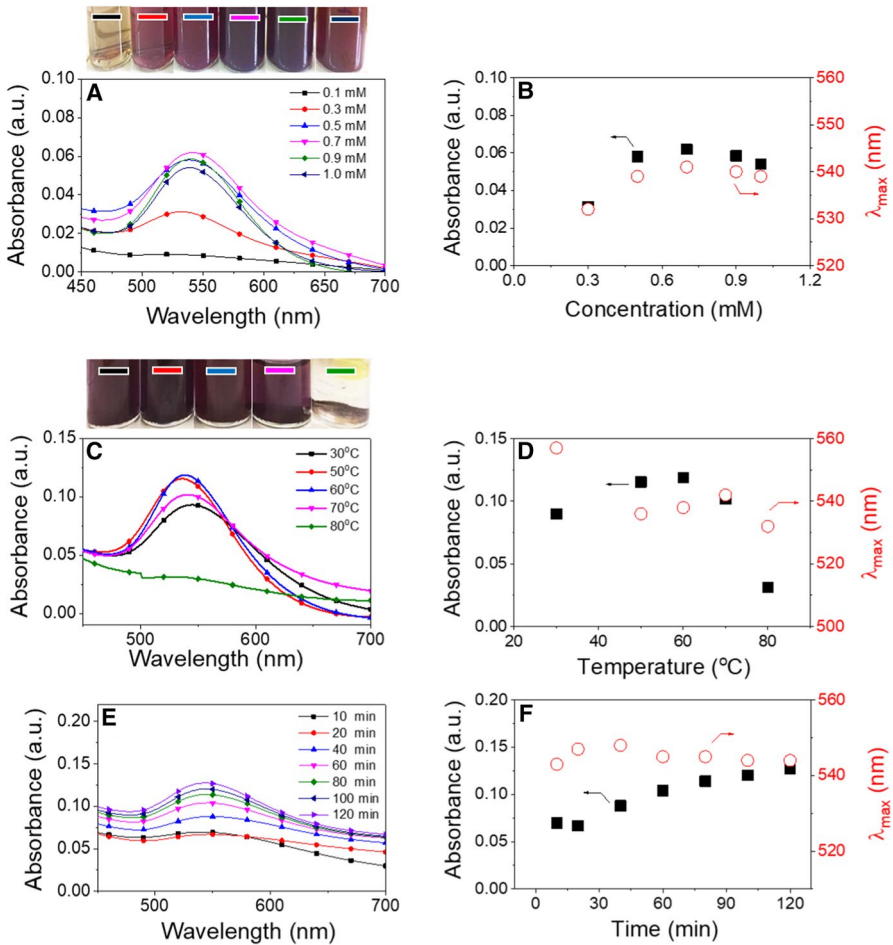
Fig. 3 UV–Vis spectra (left) and relative color change (upper photographs) and plots of parameters versus absorbance and wavelength values (right): concentration of silver ions (**A**, **B**), reaction temperature (**C**, **D**), and reaction time (**E**, **F**) for the biosynthesis of PT-AuNPs

UV–Vis spectra. Increase in the absorption intensity at the SPR peak with increasing reaction temperature and achieved at temperature of 60 °C is observed. The aggregation of the nanoparticles can be seen at high temperature (70–80 °C) that can be confirmed by discoloration of colloidal solution and rapid decrease of absorbance values. It is evident that the reduction of gold ion using PT extract is remarkably dependent on reaction temperature. Moreover, temperature-dependent morphology of the nanoparticles can be found with the significant change in wavelength values (532–558 nm).

The reduction time of gold ion was investigated in range between 10 and 120 min. As seen in Fig. 3E, and F, the slow increase of absorbance values with longer reaction time confirms slight increase of nanoparticles concentration in colloidal

solution. Additionally, the insignificant change in the λ_{max} values exhibits highly stable morphology of the nanoparticles according to the reaction time.

For further studies on physicochemical characterizations and their applications, the PT-AgNPs and PT-AuNPs were synthesized at optimal conditions including silver ion concentration of 2.0 mM, 80 °C, and 70 min; and gold ion concentration of 0.7 mM, 60 °C and 120 min.

Physicochemical characterizations

The stabilization of synthesized nanometals in the colloidal solution was evaluated via measuring zeta potentials and particle size distribution using DLS at 25 °C (Fig. 4). The result shows that great negative zeta potentials of colloidal solutions of PT-AgNPs and PT-AuNPs are found to be − 30 mV and − 39 mV, respectively. It indicates the high stabilization of the colloidal solution. The particle size distribution profiles show that the size of PT-AgNPs is much higher than the PT-AuNPs size. PT-AgNPs distributed in a broad range of 80–250 nm with a mean size of 150 nm while PT-AuNPs possessed a distribution in range of 6–80 nm with a mean size of 15 nm. The significant difference between the nanoparticles can be attributed to the different chemical components of stabilizing agents from the PT extract which can cause changes in the surface layers protecting nanoparticles.

FTIR spectra of PT-AgNPs and PT-AuNPs were used to determine the functional groups of the bioactive compounds present on the surface of nanoparticles as the stabilizing agents. The significant difference between the spectra of nanoparticles can be clearly observed in Fig. 5A. The spectrum of PT-AgNPs showed wavenumbers
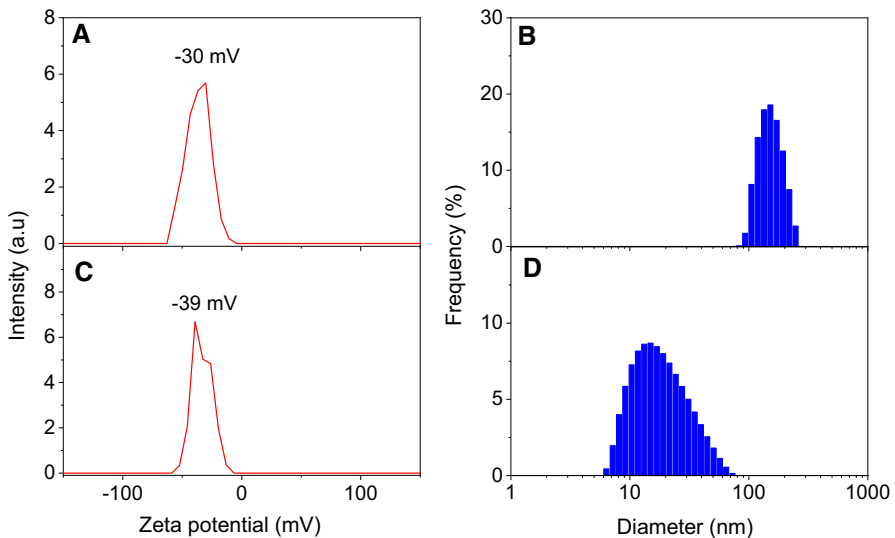

Fig. 4 Zeta potential (left) and particle distribution of DLS measurement (right): **A** and **B** PT-AgNPs and **C** and **D** PT-AuNPs
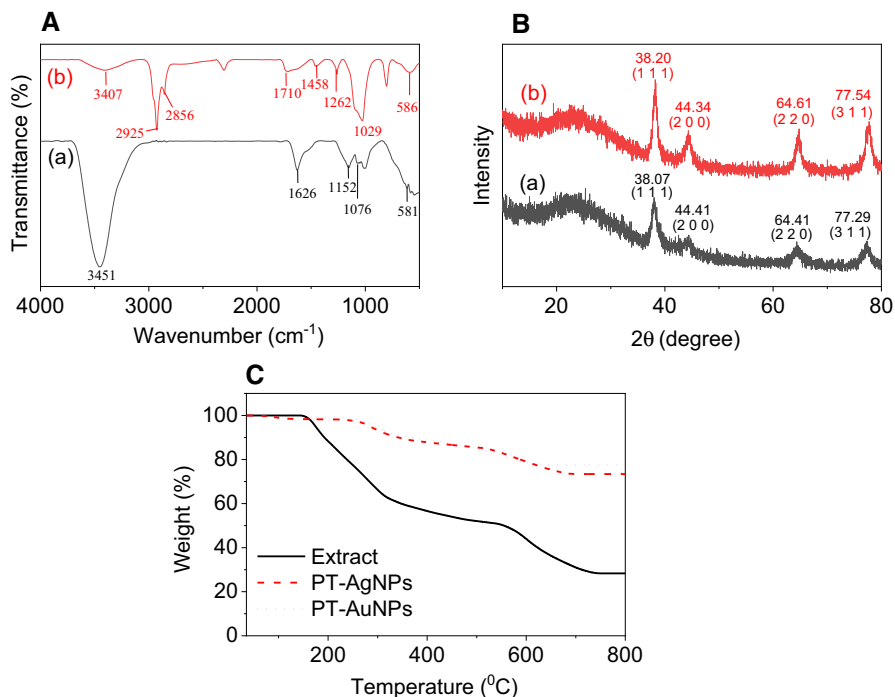
A

B

C

Fig. 5 **A** FTIR spectra of (a) PT-AgNPs and (b) PT-AuNPs; **B** XRD pattern of (a) PT-AgNPs and (b) PT-AuNPs; and **C** TGA curves of PT extract, PT-AgNPs and PT-AuNPs

at 3451, 1629, 1152, 1076, and 581 cm^{-1} while the peaks of PT-AuNPs were found at 3407, 2925, 2856, 1710, 1458, 1262, 1029, and 586 cm^{-1}. The broad peaks at 3407–3451 cm^{-1} were assigned to stretching vibrations of the O–H and N–H groups present in polysaccharides, polyphenols, and proteins, while the peaks at 2925 and 2856 cm^{-1} are attributed to stretching vibrations of C–H groups of polysaccharides [36]. The intense peaks between 1710 and 1629 cm^{-1} are related to stretching vibrations of the C=O and C=N groups in the proteins and carboxylic acids. The peak at 1458 cm^{-1} is assigned to the bending vibration of O–H groups. The peaks between 1262 and 1152 cm^{-1} correspond to the vibrations of C–N group of proteins while the peaks at 1076 and 1029 cm^{-1} are assigned to the C–O groups in polysaccharides and polyphenols. The peak around 580 cm^{-1} is related to the bending vibrations of C–C–N groups in proteins [37]. The FTIR data indicate that organic components in the PT extract correlate to the stabilizing agent of the nanoparticles. Moreover, the difference among organic components on the surface of PT-AgNPs and PT-AuNPs is in agreement with the particle size distribution determined from DLS data.

The crystalline structure of the metallic nanoparticles was determined using XRD analysis as shown in Fig. 5B. The patterns of AgNPs crystals showed Bragg reflections at 2θ peaks of 38.07°, 44.41°, 64.41°, and 77.29° relating to the face-centered cubic (fcc) planes (111), (200), (220), and (311), respectively (card no. 00-004-0783) while these fcc planes of AuNPs crystal were found at

2θ peaks of 38.20°, 44.34°, 64.61°, and 77.54°, respectively (card no. 00-004-0784). The crystalline parameters of XRD data calculated are listed in Table S1. The mean crystalline size D of the nanoparticle crystal can be estimated via the Debye–Scherrer formula,

$$D = \frac{0.9\lambda}{\beta \cos\theta} \tag{1}$$

where λ is the wavelength of the X-rays used for diffraction and β is the full width at half maximum (FWHM) in radian unit of the corresponding 2θ peak. The crystalline diameter for the fcc planes of (111), (200), (220), and (311) was calculated to be 7.55, 8.94, 5.98, and 7.82 nm, respectively, for PT-AgNPs and 8.67, 7.03, 8.87, and 8.35 nm, respectively. The mean crystal size of PT-AgNPs and PT-AuNPs was estimated to be 7.57 and 8.23 nm, respectively. On the other hand, the mean lattice constant and cell volume of PT-AgNPs were estimated to be 4.086 Å and 68.217 Å^3, respectively, while these parameters of PT-AuNPs were found to be 4.079 Å and 68.867 Å^3, respectively. This result confirms the presence of AgNPs and AuNPs crystals in the relative samples [38–40].

The thermal stability of nanoparticles was evaluated using TGA curves measured in the air atmosphere at flow rate of 20 mL/min and heating rate of 10 °C/min with sample mass of approximately 10 mg. The solid plant extract was used as a reference sample. The difference in the thermal behavior between the nanoparticles and the PT extract is clearly observed in Fig. 5C. The PT extract showed thermal stability at 160 °C and mass loss is about 48.2% in temperature stage of 160–500 °C and about 23.5% in temperature region of 500–700 °C. Meanwhile, similar thermal behavior is observed for both the synthesized nanoparticles. Indeed, their thermal stability is determined at 270 °C and the mass loss of PT-AgNPs and PT-AuNPs in temperature region of 270–650 °C is found to be 26.6% and 22.4%, respectively. The ashes remained after the heating process of the nanoparticles much greater than that of the extract are attributed to the presence of inorganic components in the synthesized samples. The result indicates that the samples contain the organic layer stabilizing the metallic nanoparticles.

The morphology and size distribution were evaluated using SEM and TEM measurements and elemental composition of the nanoparticles was determined by EDX patterns. Meanwhile, crystalline structure of the nanoparticles was studied using HR-TEM and SAED pattern. For physicochemical characterizations of the PT-AgNPs sample (Fig. 6), SEM images showed that the nanoparticles existed in cluster with uniform spherical particles and size was determined less than 20 nm. The solid EDX pattern showed strong signals at 2.99 and 3.15 keV which confirmed the presence of silver element in the sample [41]. The signals of carbon and oxygen revealed the organic components present in the synthesized nanoparticles. Mean percentage of silver mass in PT-AgNPs was estimated to be 80.5% (w/w). TEM images indicate the spherical nanoparticles with an even geometry. The narrow size distribution of PT-AgNPs was found in the range of 5–15 nm with a mean size of 10 nm that is in agreement with the XRD analysis. The HR-TEM image showed the finger spacing of 0.24 nm that correlated well to
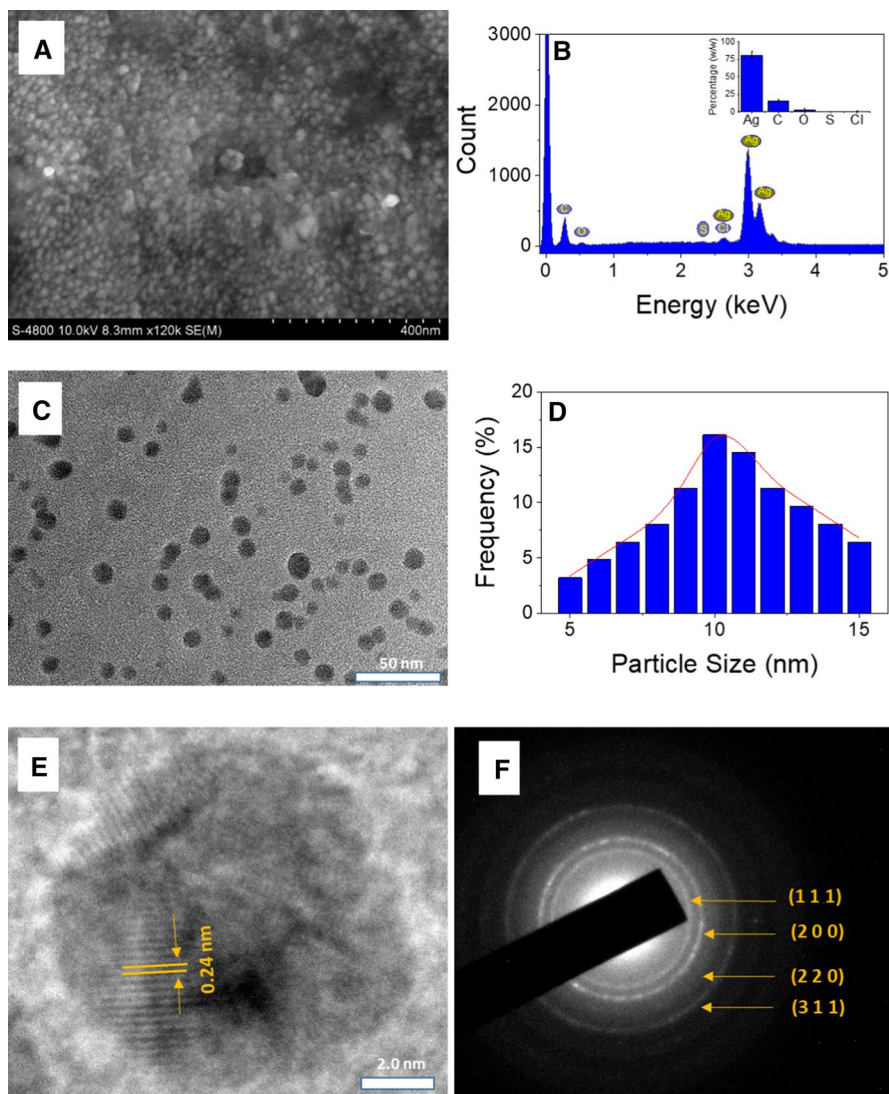
Fig. 6 **A** SEM image; **B** EDX pattern; **C** TEM image; **D** particle size distribution; **E** HR-TEM image and SAED image of PT-AgNPs

the spacing plane of (1 1 1) silver fcc (Table S1). The SAED patterns reveal the bright rings relating to (fcc) planes (1 1 1), (2 0 0), (2 2 0), and (3 1 1) that confirmed the presence of silver crystals in the PT-AgNPs.

However, the morphology properties of PT-AuNPs showed significant difference as clearly observed in Fig. 7. The SEM image revealed PT-AuNPs possessing clusters with the dissimilar particles. The solid EDX pattern confirmed the presence of gold element with 67% (w/w) in the PT-AuNPs sample. TEM images
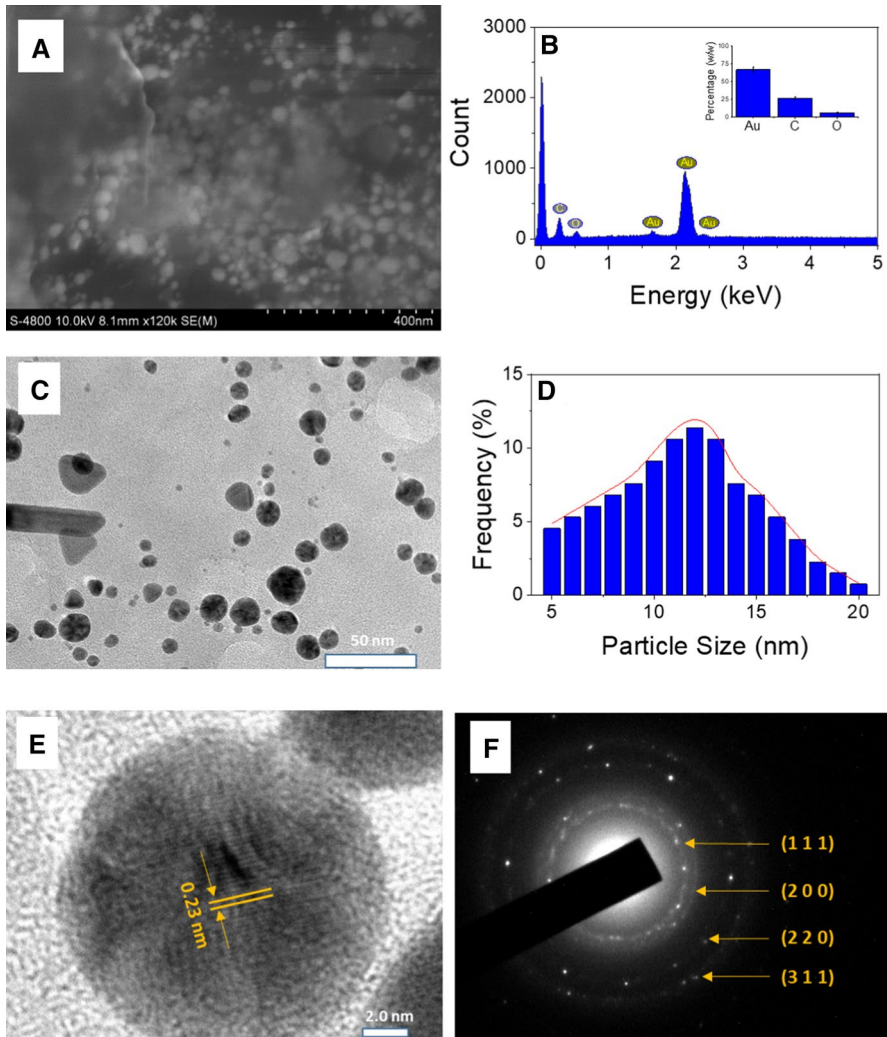
Fig. 7 **A** SEM image; **B** EDX pattern; **C** TEM image; **D** particle size distribution; **E** HR-TEM image and **F** SAED image of PT-AuNPs

showed that PT-AuNPs possessed the multiple shapes including sphere, hexagon, triangle, and rod. The size distribution is found in the range of 5–20 nm with a mean size of 12 nm which is slightly higher than the size calculated from XRD data. The HR-TEM measurement found the finger spacing 0.23 nm which is related to the fcc plane of (1 1 1) (Table S1) while the SAED patterns confirmed the gold nanoparticles in the sample.

Antibacterial activity

Antibacterial activity of the nanoparticles was evaluated against two Gram-positive bacteria including *B. subtilis* and *S. aureus* and two Gram-negative bacteria including *S. typhi* and *E. coli*. Their bioactivity was also investigated at different ratios of dilution. Ampicillin drug and Luria Bertani broth were used as positive and negative references, respectively. The PT extract and the PT-AuNPs showed no inhibition against all tested strains even at the highest concentrations. The low bioactivity of AuNPs biosynthesized from plant extract has been reported in literature [42, 43]. Notably, PT-AgNPs showed strong antibacterial activity against all the test microorganisms. The antibacterial effect and plots of inhibition zone versus varied ratios of dilution are illustrated in Fig. 8. The images revealed that inhibition circle decreases with increasing dilution ratios and PT-AgNPs possessed the different bioactivity against the tested strains. The zone of inhibition at the highest concentration (1:1, v/v) was in order of *E. coli* (15 mm), *B. subtilis* (13 mm), *S. typhi* (10 mm), and *S. aureus* (10 mm). It is well known that the AgNPs can anchor to cell wall of bacterium and inducing structural changes in the cell membrane and the permeating it to kill the cell [44, 45]. Due to the difference of cell wall between microorganisms, the bacterial activity of AgNPs is strongly dependent on the various strains. The excellent ability preventing bacterial infections is believed that PT-AgNPs can be effectively used for medical treatments such as wound dressings, dental diseases, and bond cements.

Catalysis activity

Due to the urgent demands for the removal of toxic pollutants, the degradation of these contaminants into non-toxic products using the chemical reagents such as $NaBH_4$ or H_2O_2 has been frequently investigated in recent years [46, 47]. It is well known that the catalytic reduction of NiPs and RhB using heterogeneous nanometals without leaching metallic atom into the solution is followed by the Langmuir–Hinshelwood model [48]. The catalytic model can be described via the electron transfer on surface of heterogeneous nanocatalyst as shown in Fig. 9. In this mechanism, borohydrate ions are adsorbed onto the surface of metal nanoparticles and then electron transferred into the surface of metal nanoparticles. Due to very excessive amount of $NaBH_4$ used in comparison with the dye concentrations and catalysts, the adsorption of borohydrate ions is assumed to be an irreversible process. In the next process, the electrons are transferred from nanocatalyst surface into the dyes which are adsorbed via an equilibrated process and then the reduction products are formed by the detachment. It should be noted that the adsorption of dyes on surface of metal
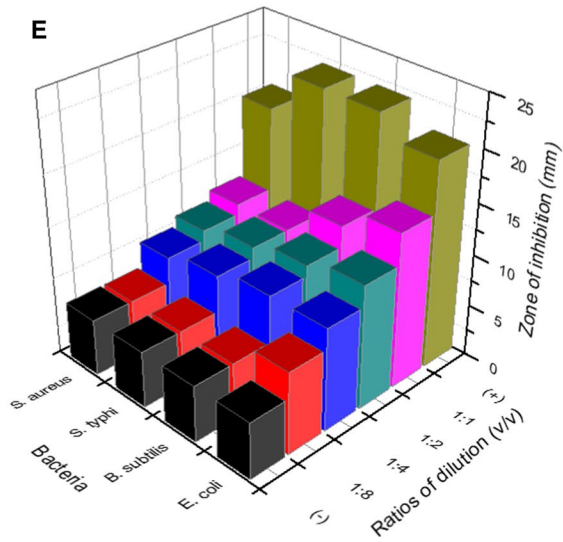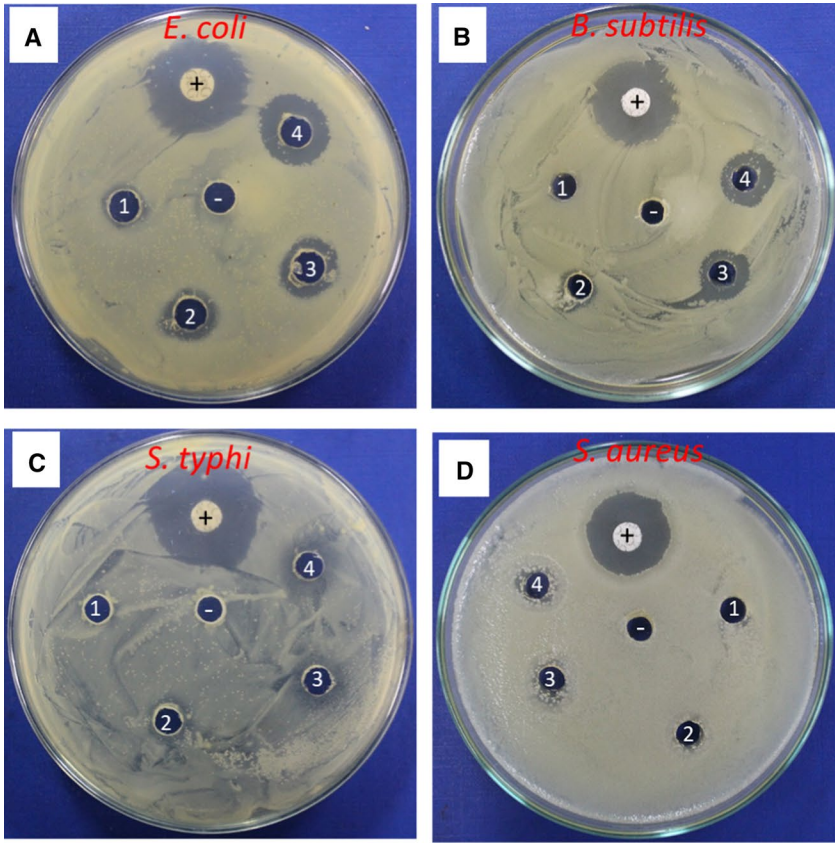
nanoparticles is reversible via the Langmuir isotherm which is major factor affected the rate of reduction reaction. Otherwise, the reaction rate is mainly dependent on the catalyst surface areas which are related to the adsorption of the substrates. In the present work, the rate constants in various nanocatalyst doses (1–5 µL) were thus investigated with assumed reaction kinetic following pseudo-first order with respect to substrate concentration. The reaction rate is expressed as follows:

$$r_t = -\frac{dC_{dye}}{dt} = k_{app}C_{dye} \tag{2}$$

where k_{app} is apparent reaction rate constant and has units of s^{-1}. Integrating Eq. (2), we obtain Eq. (3).

$$\ln\left(\frac{C_{dye0}}{C_{dye}}\right) = k_{app}t \tag{3}$$

Thus, a plot of $\ln(C_{dye0}/C_{dye})$ versus reaction time results a straight line, and its slope is used to estimate values k_{app}.
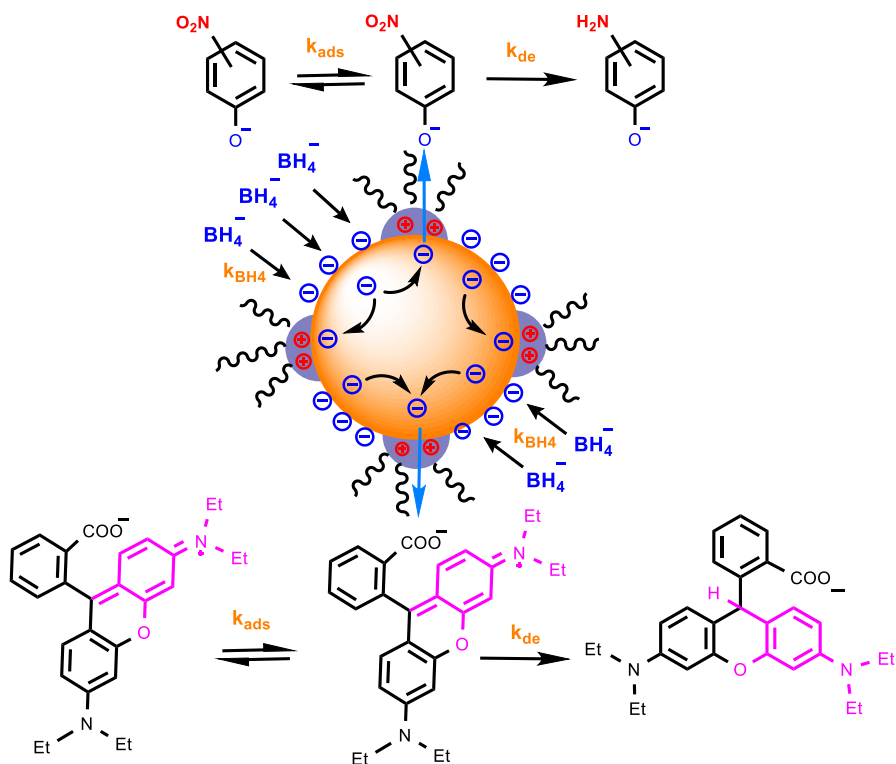

Fig. 9 Schematic representation of the catalytic reduction of NiPs and RhB using heterogeneous metallic nanoparticles catalyst via the Langmuir–Hinshelwood model. The abbreviations including k_{BH4}, k_{de}, and k_{ads} are rate constants of BH$_4$ adsorption, detachment of the product, and NiP adsorption, respectively

The kinetics of reduction reaction in the presence of nanocatalysts were in situ monitored by measurement of UV–Vis spectroscopy. Discoloration of dye solutions and decrease of absorption intensity at corresponding peaks in UV–Vis spectra confirmed good yields of the contaminant reduction. The spectra are shown in Figs. S2–S7. Degradation in absorbance values is observed at relative peaks of 414 nm, 391 nm, and 553 nm for 2-NiP, 3-NiP, and RhB, respectively. The enhancement of reaction performance might be confirmed by the reduction of reaction time with increasing doses of the catalysts. However, the reaction rate is significantly dependent on substrate structure and the metallic nanoparticles used. Indeed, the yield of 2-NiP reduction in the presence of PT-AgNPs is recognized approximately 68% in 19 min at 1 μL catalyst and approximately 74% in 13 min at 5 μL catalyst; while in the presence of PT-AuNPs, the 2-NiP reduction performance is slightly increased from approximately 77% in 20 min at 1 μL catalyst and approximately 79% in 15 min at 5 μL catalyst. Meanwhile, a dissimilar trend was observed for the reduction of 3-NiP which showed better catalytic efficiency of PT-AgNPs in comparison with PT-AuNPs. The reduction performance is increased from approximately 81% in 15 min at 1 μL PT-AgNPs and approximately 86% in only 6 min at 5 μL PT-AgNPs while catalytic performance of PT-AuNPs is observed approximately 81% in 23 min at 1 μL and approximately 81% in 10 min at 5 μL. The degradation of RhB dye showed that the reaction time is significantly slower than the reduction of NiPs. The reduction yield in the presence of PT-AgNPs is approximately 84% in 10 min at 5 μL while this yield is approximately 81% in 36 min at 5 μL PT-AuNPs. It is clearly that property of metallic nanoparticles and dose of nanocatalyst strongly effected on the reaction time of relative pollutant reduction.

The kinetic investigation was performed at the different doses of nanocatalyst as presented in Fig. 10 and summarized in Table 1. The reaction rate constants against the doses of the colloidal nanocatalyst solution are also plotted to observe influence of reaction rate on number of the nanoparticles (Fig. 10G). The results showed good linear correlations between $\ln(C_0/C_t)$ and the reaction time which coincides with a pseudo-first-order mechanism for degradation of all pollutants. The reduction of 2-NiP found the rate constants in narrow ranges of 1.11×10^{-3} s^{-1} to 1.77×10^{-3} s^{-1} with values R^2 of 0.939 to 0.982 for PT-AgNPs and 1.30×10^{-3} s^{-1} to 1.83×10^{-3} s^{-1} with values R^2 of 0.915 to 0.991 for PT-AuNPs with increase of the nanocatalyst doses (1–5 μL). Also, Fig. 10G shows that there is no influence of the nanometal kinds on the 2-NiP reduction but the nanocatalyst number can slightly improve the reduction efficiency. Meanwhile, the reduction of 3-NiP showed the clear effect of nanocatalyst doses on the reduction yields which found a wide range of apparent rate constants obtained with the increase of nanocatalyst number. The rate constants of PT-AgNPs catalyst were found to be 1.50×10^{-3} s^{-1} to 4.98×10^{-3} s^{-1} with correlation coefficient of 0.941 to 0.964 s^{-1} and the reduction in the presence of PT-AuNPs catalyst showed the value k_{app} in range of 1.15×10^{-3} s^{-1} to 2.99×10^{-3} s^{-1} with correlation coefficient of 0.950 to 0.991 s^{-1}. This result also revealed that the catalytic activity of PT-AgNPs is better than that of PT-AuNPs for the reduction of 3-NiP. As seen in Fig. 10G, the rate constant values found in the reduction of both NiPs are similar at low catalyst doses (1–2 μL); however, these values of 3-NiP reduction are rapidly increasing at high doses. It can be because at great numbers of
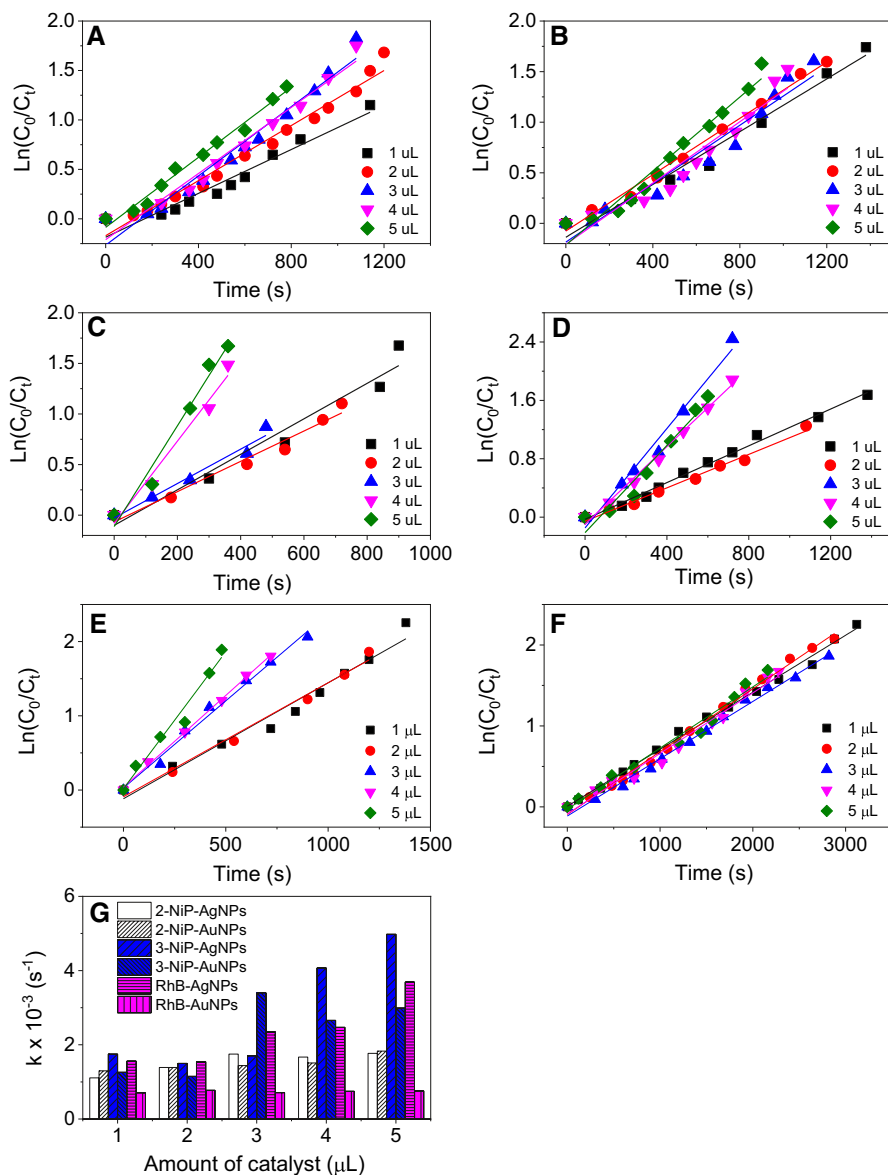
Fig. 10 pseudo-first-order kinetic model in concentration changes of PT-AgNPs (left) and PT-AuNPs (right) for reduction of 2-NiP (**A** and **B**), 3-NiP (**C** and **D**) and RhB (**E** and **F**) and plots of rate constant versus amount of the nanocatalysts (**G**)

nanoparticles, the nitro group at 3-position in 3-NiP structure might induce increase of nitrophenolate adsorption rate (k_{ads}) onto surface of nanocatalyst compared to the 2-position. Otherwise, intramolecular hydrogen bonding between nitro and hydroxyl groups in 2-NiP molecule obstructs adsorption process of nitrophenolate ions and

Table 1 Rate constants derived from the kinetic experiments conducted at different concentrations of PT-AgNPs and PT-AuNPs for catalytic reduction of dyes

Com	Cat	Volume of nanoparticle solutions									
		1 μL		2 μL		3 μL		4 μL		5 μL	
		$kx10^{-3}$	R^2	$kx10^{-3}$	R^2	$kx10^{-3}$	R^2	$kx10^{-3}$	R^2	$kx10^{-3}$	R^2
2-NiP	AgNPs	1.11	0.939	1.39	0.975	1.75	0.957	1.67	0.963	1.77	0.982
	AuNPs	1.30	0.972	1.39	0.991	1.44	0.940	1.51	0.915	1.83	0.960
3-NiP	AgNPs	1.75	0.941	1.50	0.964	1.70	0.958	4.07	0.962	4.98	0.964
	AuNPs	1.26	0.991	1.15	0.985	3.40	0.973	2.66	0.990	2.99	0.950
RhB	AgNPs	1.56	0.967	1.54	0.985	2.35	0.987	2.47	0.998	3.69	0.970
	AuNPs	0.70	0.995	0.78	0.994	0.71	0.991	0.75	0.978	0.76	0.981

thus leads to low reduction performance. The catalysts showed an excellent performance of NiPs reduction compared with nanometals previously reported in the literature [49–52].

For the degradation of RhB, the plots of rate constants versus the nanocatalyst showed different behaviors of PT-AgNPs and PT-AuNPs catalysts. Catalytic performance rapidly increased with increasing PT-AgNPs doses whereas this performance has almost no effect on PT-AuNPs doses in the range of 1–5 μL. The apparent rate constants using PT-AgNPs catalyst are found in range of 1.54×10^{-3} s^{-1} to 3.69×10^{-3} s^{-1} with value R^2 of 0.967 to 0.998 while these rate constants for PT-AgNPs catalyst are as low as 0.70×10^{-3} s^{-1} to 0.78×10^{-3} s^{-1} with value R^2 of 0.978 to 0.995. The results reveal that the catalytic efficiency of PT-AgNPs is much better than that of PT-AuNPs in degradation of RhB. In comparison of catalytic performance with the nanometals in the literature, this work showed a high catalytic efficiency in degradation of RhB [53–55].

Conclusions

The green, low-cost, and simple synthesis of silver and gold nanoparticles was effectively carried out using the aqueous extract of *Phlogacanthus turgidus* leaves. The characterization of biogenic nanoparticles was well identified by analysis techniques. The crystalline PT-AgNPs existed in spherical shape with a mean size of 10 nm while crystalline PT-AuNPs was identified in the multiple shape with a mean size of 12 nm. The antibacterial activity showed that PT-AgNPs were a potential antibacterial agent against four bacterial strains including *E. coli*, *B. subtilis*, *S. typhi*, and *S. aureus.* Their catalytic activity has been evaluated for the reduction of NiPs and RhB. The investigation on the reaction kinetics revealed that the metallic nanoparticles are effective catalysts for application in environmental treatment. The rate constants confirmed that catalytic activity of PT-AgNPs was better than that of PT-AuNPs and the reduction performance of 3-NiP was the highest in the tested

pollutants. The biogenic metallic nanoparticles indicated a highly potential with a wide application in biology and catalysis.

Data availability The data used to support the findings of this study are included within the article.

Declarations

Conflicts of interest The authors declare that they have no conflict of interest.

References

1. A. Lateef, J.A. Elegbede, P.O. Akinola, V.A. Ajayi, Pan Afr. J. Life Sci **3**, 157 (2019)
2. P.D. Shankar, S. Shobana, I. Karuppusamy, A. Pugazhendhi, V.S. Ramkumar, S. Arvindnarayan, G. Kumar, Enzyme Microb. Technol. **95**, 28 (2016)
3. J.J. Soldevila-Barreda, N. Metzler-Nolte, Chem. Rev. **119**, 829 (2019)
4. P.K. Dikshit, J. Kumar, A.K. Das, S. Sadhu, S. Sharma, S. Singh, P.K. Gupta, B.S. Kim, Catalysts **11**, 902 (2021)
5. A.K. Saim, P.C.O. Adu, R.K. Amankwah, M.N. Oppong, F.K. Darteh, A.W. Mamudu, Environ. Technol. Rev. **10**, 111 (2021)
6. K. Khurana, N. Jaggi, Plasmonics **6**, 981 (2021)
7. B. Unnikrishnan, C.-W. Lien, H.-W. Chu, C.-C. Huang, J. Hazard. Mater. **401**, 123397 (2021)
8. M.Z. Salem, E.-H. Mervat, H.M. Ali, A. Abdel-Megeed, A.A. El-Settawy, M. Böhm, M.M. Mansour, A.Z. Salem, Microb. Pathogen. **158**, 105107 (2021)
9. S.S. Salem, A. Fouda, Biol. Trace Elem. Res. **199**, 344 (2021)
10. M.-T. Tran, L.-P. Nguyen, D.-T. Nguyen, L. Cam-Huong, C.-H. Dang, T.T.K. Chi, T.-D. Nguyen, Res. Chem. Intermed. **47**, 4613 (2021)
11. Z. Khiya, Y. Oualcadi, E.H. Mourid, I. Tagnaout, F. Berrekhis, T. Zair, F. El Hilali, Res. Chem. Intermed. **47**, 3131 (2021)
12. M. Arif Asghar, R. Ismail Yousuf, M. Harris Shoaib, N. Mumtaz, BIO Integr. **2**, 71–78 (2021)
13. X. Zhu, E. Blanco, M. Bhatti, A. Borrion, Sci. Total Environ. **757**, 143747 (2020)
14. Y. Anwar, I. Ullah, B.O. AlJohny, A.M. Al-Shehri, E.M. Bakhsh, M. Ul-Islam, A.M. Asiri, T. Kamal, Appl. Nanosci. (2021).
15. R. Mythili, P. Srinivasan, L. Praburaman, M.M. Al-Ansari, L. Al-Humaid, S. Vijayalakshmi, T. Selvankumar, Appl. Nanosci. (2021).
16. P. Subramaniam, K. Nisha, A. Vanitha, M.L. Kiruthika, P. Sindhu, B.H. Elesawy, K. Brindhadevi, K. Kalimuthu, Appl. Nanosci. (2021).
17. A.A. Yaqoob, T. Parveen, K. Umar, M.N. MohamadIbrahim, Water **12**, 495 (2020)
18. Y. Yang, X. Li, C. Zhou, W. Xiong, G. Zeng, D. Huang, C. Zhang, W. Wang, B. Song, X. Tang, Water Res. **184**, 116200 (2020)
19. R. Saxena, M. Saxena, A. Lochab, ChemistrySelect **5**, 335 (2020)
20. Y. Fu, P. Xu, D. Huang, G. Zeng, C. Lai, L. Qin, B. Li, J. He, H. Yi, M. Cheng, Appl. Surf. Sci. **473**, 578 (2019)
21. J.P. Peesa, P.R. Yalavarthi, A. Rasheed, V.B.R. Mandava, J. Acute Dis. **5**, 364 (2016)
22. M.J. Vaidya, S.M. Kulkarni, R.V. Chaudhari, Org. Process Res. Dev. **7**, 202 (2003)
23. S. Khan, M. Naushad, A. Al-Gheethi, J. Iqbal, J. Environ. Chem. Eng. **9**, 106160 (2021)
24. F. Lu, D. Astruc, Coord. Chem. Rev. **408**, 213180 (2020)
25. M.H. Oueslati, L. Ben Tahar, A.H. Harrath, Green Chem. Lett. Rev. **13**, 18–26 (2020)

26. S. Marimuthu, A.J. Antonisamy, S. Malayandi, K. Rajendran, P.-C. Tsai, A. Pugazhendhi, V.K. Ponnusamy, J. Photochem. Photobiol. B **205**, 111823 (2020)
27. A.A. Yaqoob, K. Umar, M.N.M. Ibrahim, Appl. Nanosci. **10**, 1369 (2020)
28. L. David, B. Moldovan, Nanomaterials **10**, 202 (2020)
29. X.-H. Yuan, B.-G. Li, X.-Y. Zhang, H.-Y. Qi, M. Zhou, G.-L. Zhang, J. Nat. Prod. **68**, 86 (2005)
30. M.D. Tri, N.T. Phat, N.T. Trung, C.-T.D. Phan, P.N. Minh, M.T. Chi, T.-P. Nguyen, C.H. Dang, L. Hong Truong, N.K.T. Pham, J. Asian Natural Prod. Res. **24**, 1 (2021)
31. N.T. Phat, M.T. Chi, P.N. Minh, D.C. Hien, M.D. Tri, Sci. Technol. Dev. J. **5**, 1 (2021)
32. Y.Y. Loo, Y. Rukayadi, M.-A.-R. Nor-Khaizura, C.H. Kuan, B.W. Chieng, M. Nishibuchi, S. Radu, Front. Microbiol. **9**, 1555 (2018)
33. E. Hoseinzadeh, P. Makhdoumi, P. Taha, H. Hossini, J. Stelling, M. AmjadKamal, Current Drug Metab. **18**, 120–128 (2017)
34. S. Ahmed, M. Saifullah, B.L. Ahmad, S. Swami, J. Radiat. Res. Appl. Sci. **9**, 1–7 (2016)
35. H. Erjaee, H. Rajaian, S. Nazifi, Adv. Nat. Sci. **8**, 025004 (2017)
36. D. MubarakAli, N. Thajuddin, K. Jeganathan, M. Gunasekaran, Colloids Surf. B **85**, 360 (2011)
37. T. Suman, S.R. Rajasree, A. Kanchana, S.B. Elizabeth, Colloids Surf. B **106**, 74 (2013)
38. M. Bindhu, M. Umadevi, Spectrochim. Acta Part A Mol. Biomol. Spectrosc. **101**, 184 (2013)
39. M. Bindhu, M. Umadevi, Mater. Lett. **120**, 122 (2014)
40. V.-D. Doan, Q.-H. Pham, B.-A. Huynh, A.-T. Nguyen, T.-D. Nguyen, J. Environ. Chem. Eng. **9**, 106590 (2021)
41. M. Vijayakumar, K. Priya, F. Nancy, A. Noorlidah, A. Ahmed, Ind. Crops Prod. **41**, 235 (2013)
42. V.-D. Doan, M.-T. Phung, T.L.-H. Nguyen, T.-C. Mai, T.-D. Nguyen, Arab. J. Chem. **13**, 7490 (2020)
43. T.M.-T. Nguyen, T.A.-T. Nguyen, N. Tuong-Van Pham, Q.-V. Ly, T.T.-Q. Tran, T.-D. Thach, C.-L. Nguyen, K.-S. Banh, V.-D. Le, L.-P. Nguyen, Arab. J. Chem. **14**, 103096 (2021)
44. S. Prabhu, E.K. Poulose, Int. Nano Lett. **2**, 1 (2012)
45. N. Durán, M. Durán, M.B. De Jesus, A.B. Seabra, W.J. Fávaro, G. Nakazato, Nanomedicine **12**, 789 (2016)
46. R. Javaid, U.Y. Qazi, Int. J. Environ. Res. Public Health **16**, 2066 (2019)
47. K. Naseem, Z.H. Farooqi, R. Begum, A. Irfan, J. Clean. Prod. **187**, 296 (2018)
48. M.B. Wazir, M. Daud, F. Ali, M.A. Al-Harthi, J. Mol. Liquids **315**, 113775 (2020)
49. S.M. Albukhari, M. Ismail, K. Akhtar, E.Y. Danish, Colloids Surf. A **577**, 548 (2019)
50. M. Gondwal, G. Joshi nee Pant, Int. J. Biomater. **2018**, 6735426 (2018)
51. P. Kaithavelikkakath Francis, S. Sivadasan, A. Avarachan, A. Gopinath, Part. Sci. Technol. **38**, 365 (2020)
52. L. Sun, H. Li, P. Lv, J. Chen, J. Inorg. Organomet. Polym Mater. **29**, 269 (2019)
53. A. Velidandi, N.P.P. Pabbathi, R.R. Baadhe, J. Mol. Struct. **1236**, 130287 (2021)
54. T. Sowmyya, J. Environ. Chem. Eng. **6**, 3590 (2018)
55. R. Vinayagam, T. Varadavenkatesan, R. Selvaraj, Green Process. Synth. **7**, 30 (2018)

Publisher's Note Springer Nature remains neutral with regard to jurisdictional claims in published maps and institutional affiliations.